# Optical, electronic and magnetic property tuning of boron nitride nanosheets with oxygen doping and functionalization

**Qunhong Weng,[1]* Dmitry G. Kvashnin,[2,3]* Xi Wang,[4] Ovidiu Cretu,[1] Yijun Yang,[4] Min Zhou,[1] Chao Zhang,[1,5] Dai-Ming Tang,[1] Pavel B. Sorokin,[2,6] Yoshio Bando[1] & Dmitri Golberg [1,5,7]***

[1]International Center for Materials Nanoarchitectonics (MANA), National Institute for Materials Science (NIMS), Namiki 1-1, Tsukuba, 305-0044, Japan. Email: weng.qunhong@nims.go.jp; golberg.dmitri@nims.go.jp

[2]National University of Science and Technology (MISIS), 119049, Leninskiy prospekt 4, Moscow, Russia. Email: dgkvashnin@gmail.com

[3]Emanuel Institute of Biochemical Physics RAS, 119334, Kosigina st. 4, Moscow, Russian Federation

[4]School of Science, Beijing Jiaotong University, Beijing, P. R. China

[5]University of Tsukuba, Tennodai 1-1, Tsukuba, Ibaraki, 3058577, Japan

[6]Technological Institute for Superhard and Novel Carbon Materials, 108840, Moscow, Troitsk, Centralnaya st. 7a, Russian Federation

[7]Queensland University of Technology, 2 George St., Brisbane, QLD 4000, Australia

**Engineering of optical, electronic and magnetic properties of hexagonal boron nitride (*h*-BN) nanomaterials *via* oxygen doping and functionalization has been envisaged in theory. However, it is still unclear to what extent these properties can be alternated using such methodology because of lack of significant experimental progresses and systematic theoretical investigations. Therefore, herein, we provide comprehensive theoretical predictions verified by solid experimental confirmations which unambiguously answer this long-standing question. We report on narrowing of the optical band gap in *h*-BN nanosheets (from ~5.5 eV down to 2.1 eV) and appearance of paramagnetism and photoluminescence (of both Stokes and anti-Stokes types) in them after oxygen doping and functionalization. These results are highly valuable for further advances in semiconducting nanoscale electronics, optoelectronics and spintronics.**

The energy band gap plays the crucial role in solid state materials' optical and electronic properties. Design of artificial materials with suitable band gaps is of high priority in many fields, *e.g.* photovoltaics, electronics, sensing, photosynthesis, photoluminescence *etc.*[1-3] Heteroatom-doping has usually been adopted for the electronic property tuning in solid state physics[4,5]. In theory, alloying of wide-band-gap *h*-BN (5.5 eV) and semi-metallic graphene (0 eV) within a 2D atomic monolayer would lead to a widely tunable band gap in such newly formed ternary hexagonal B–C–N system. Although being very intriguing, such concept meets many

experimental difficulties because homogeneous mixing of BN and C phases in a honeycomb-like lattice is a thermodynamically unfavourable process. Thus BN and graphene components always tend to separate under high temperature[6,7]. This fact limits the structural diversity of BCN alloys for precise electronic and/or other property adjustments.

Alternatively, introduction of oxygen atoms into a *h*-BN lattice provides a new practical route for its band gap and magnetic property engineering[8]. In fact, theoretical simulations have documented that the band gaps of BN nanotubes (BNNTs) and BN nanosheets can be narrowed by replacing N atoms with O atoms[9,10]. At the same time, their optical, electronic, and magnetic properties could be varied through such substitution method, as was also predicted in several theoretical works[10-13]. In the previous experiments the embedment of oxygen atoms into the *h*-BN honeycomb-like lattice has indeed been confirmed under atomic resolution using annular dark-field (ADF) scanning transmission electron microscopy (STEM) by Krivanek and coworkers[14]. Teo *et al*. have found that the optical band gap of BN nanosheets is reduced to 4.31 eV and the conductivity is improved by 2 orders of magnitude after oxygen plasma treatment[15]. More recently, Lee *et al*., and also our group, have reported that the edge-functionalized BN exhibits adsorption in UV and near UV regions[16,17]. These progresses indicate that, instead of carbon, oxygen functionalization is an alternative and rather practical strategy for *h*-BN electronic band structure tuning. Besides oxygen, many other heteroatoms and functional groups have also been thought to be able to modulate the band gaps of *h*-BN, including H, F, *etc*.[18,19] However,

these heteroatoms and functional groups are unable to be perfectly incorporated into the BN honeycomb-like lattice.

In this work, we performed step-by-step explorations of different oxygen functionalization/doping mode impacts onto the *h*-BN monoatomic layer electronic band structures, including *h*-BN interior substitution and edge hydroxylation. First, the density functional theory (DFT) simulations predicted narrowing of the energy band gap in a BNO monolayer to 1.7 eV under incorporation of 25 at.% of oxygen. This prediction was then verified experimentally: we successfully synthesized a yellow-coloured boron oxynitride with a high oxygen content, measured as 23.1 at.%, and proved that its optical band gap was indeed reduced to 2.1 eV, as compared with the standard *h*-BN material (~5.5 eV). A rich variety of the spectroscopic methods, such as X-Ray Diffraction (XRD), Fourier Transform Infrared Spectroscopy (FT-IR), X-ray Absorption Near Edge Structure Spectroscopy (XANES), X-ray Photoelectron Spectroscopy (XPS), Electron Paramagnetic Resonance Spectroscopy (EPR), and Electron Energy Loss Spectroscopy (EELS), together with DFT simulations, were then applied to uncover the structure of the prepared BNO nanomaterial. Oxygen atoms were proved to either substitute for nitrogen atoms in a BN honeycomb-like lattice or initiate the edge hydroxylation, thus forming a very stable structure. The regarded functionalization mode was also the origin of the paramagnetic property appearance in the BNO system, as was for the first time observed in the experiments. The employed herein novel band gap and magnetic engineering methodology opens up a practical way

to design and fabricate small-band-gap and stable nanoscale BN semiconductors for various optical, electrical, magnetic and energy harvesting/conversion applications.

## Results

### Theoretical predictions of *h*-BN band gap tuning *via* oxygen doping and functionalization

We used DFT-PBE -PAW formalism for material band structure calculations, the details are provided in the experimental section. The calculated band gap for a standard 2D infinite *h*-BN monolayer was 4.56 eV, in agreement with other reports[20,21]. It is noted that the theoretically derived band gap values (by DFT) are underestimated compared with the experimental figures owing to electron self-interaction error[22]. Fig. 1b shows the dependence of the calculated band gap values for the periodical monolayered BNO nanosheets *versus* in-plane oxygen doping contents. We firstly consider a regular random substitutional mode (substitution of N with O atom) instead of other special arrangements, such as formation of O-B-O chains. The calculated band gaps reduced monotonically from 4.56 to 4.34 eV with increasing O content from 0 to 16.7 at.%. The case of substitution on B sites was excluded because it would cause the structural deformations and instability of a BN sheet[9]. Through the oxygen substitution, the electronic properties of BNO nanosheets are changed accordingly (for more details see Supplementary Fig. S1). At a low oxygen concentration (5 at.%), the oxygen doped layers lie deep in the conduction band (>5 eV). These states mainly come from the N electronic states in the valence bands (VB) and the B states

in the conduction bands (CB). These are responsible for the formation of direct band gaps at the Γ-point. For a BNO nanosheet containing 10 at.% of oxygen, additional unpaired electrons appear in the system. These play the major role and lead to the Fermi level increase.

A periodic 2D BNO structure with 20 at.% of oxygen dopants exhibits the limited stability owing to an unavoidable formation of O-B-O chains/domains that are restrained in a honeycomb BN lattice. These would also lead to much larger band gaps, up to 5.1 eV, for the investigated structures (see Supplementary Fig. S2), and could explain many reported wide-band-gap BNO systems[11,23,24]. Detailed information related to the investigation of the electronic properties of BNO nanostructures with special arrangements of in-plane substituted oxygen atoms can be found in Supplementary Fig. S2).

In addition to the in-plane substitution, oxygen could also been introduced through the nanosheet edge functionalization, such like *via* hydroxylation with –OH groups[16,17]. This is also an efficient way for reducing the band gap of BN materials compared with out-of-plane hydroxylation[25]. Thus we considered a finite BNO monolayer model (nanoflake) where the edges are functionalized with conjugated –OH groups (Fig. 1c). The oxygen concentration in this ~4.2 nm-sized nanosheet is 12.5 at.% (oxygen atoms are placed solely at the edges in line with the considered –OH groups). From the calculated HOMO and LUMO levels of such structure the presence of electron states with the Fermi energy is found. The nearest band energy gap is calculated to be 3.8 eV; that is much smaller than those in the original 2D *h*-BN and BNO

nanosheets. Further combination of the in-plane oxygen substitution and edge functionalization with –OH groups extends the oxygen concentration up to 25 at.%, as shown in Fig. 1d. As expected, the HOMO-LUMO energy gap of the BNO nanosheet with 25 at.% of oxygen is further reduced, down to 1.7 eV (Fig. 1d). Such low value of the energy gap makes this nanosheet an excellent material for light absorption in the UV and visible wavelength ranges.

**Synthesis and characterizations of narrow-band-gap boron oxynitride**

We then prepared the BNO samples through a solid reaction between boric acid and organic tertiary amine (Hexamethylenetetramine, HMTA) at 1000 ℃ in ammonia atmosphere. Scanning electron microscopy (SEM) and transmission electron microscopy (TEM) images of the powder-like products (Fig. 2a,b) reveal a flake-like morphology with the sizes of individual flakes varying from sub-micrometer to over 10 micrometers. High resolution TEM (HRTEM) image and XRD pattern of the product uncover the layered nature of the material, which is similar to our earlier reports on porous BN solids[26,27]. The specific surface area of this BNO sample reaches 561 $m^2 g^{-1}$, as characterized by $N_2$ adsorption-desorption measurements (Supplemenraty Fig. S6).

Qualitative EDX elemental analysis confirms the presence of B, N and O with very marginal C impurities in the product, as depicted in Fig. 2c. Further comprehensive analysis gives the detailed contents of each element (inset of Fig. 2c); there is a very high oxygen component (23.1 at.%) in the product. To understand the relative distributions of these elements, EELS and EDX mapping

were conducted (Supplementary Fig. S7). The results show that oxygen generally follows the spatial distributions of B and/or N species. We did not notice higher oxygen concentrations at the layer structure edges compared with its interior portions.

Infrared spectroscopy (IR) was used to further in depth understand the bonding nature of the prepared BNO sample. Besides the main B-N stretching vibration mode located at 1369 $cm^{-1}$, there are additional strong absorption peaks at 1092 and 3410 $cm^{-1}$, which are ascribed to $sp^2$-hybridized B-O bending and O-H stretching vibrations, respectively[17]. It is noted that the observed B-O bending vibration arises from both interior and edge conjugated B-O bonds; these are ~100 $cm^{-1}$ shifted toward lower frequencies compared with those of $B_2O_3$[28,29]. This is also in contrast to the $sp^3$ hydroxylation mode on the BN sheet surfaces, which do not show active B-O vibrations at the corresponding locations[25].We then simulated vibration frequencies of a 2D periodical BNO structure with 10 at.% of in-plane oxygen dopants. The results fit well the experimental spectrum, as illustrated in Fig. 2e. Furthermore, we have also investigated the effects of substituted oxygen concentration on the IR vibration frequencies. As shown in Supplementary Fig. S8, from 5 to 20 at.% oxygen substitution levels, only the 10 at.% doping model follows the observed experimental frequencies. This result tells us that the doping oxygen level of 10 at.% for the sample in-plane sites looks reasonable.

The presence of B-O bonds in the BNO product was also confirmed by X-ray Absorption Near Edge Structure (XANES) and XPS spectroscopies. In B K-edge XANES (Fig 2f), the first sharp

peak at 191.7 eV corresponds to the X-ray photoexcitation of B1s electrons to π* ($BN_3$). Broad peaks at 196.5-201.0 and 202.0-205.0 eV are B1s → σ* ($BN_3$) transitions. Compared with h-BN, there are additional transitions located at 192.3 and 193.5 eV for the synthesized boron oxynitride, corresponding to B1s → oxygen-replaced $BN_2O$ and $BO_3$ π* orbitals, respectively. The presence of conjugated $BN_2O$ structure verifies the embedment of O atoms into the *h*-BN lattice at the original N positions. The peak at 193.5 eV was originated from B1s → π* ($BO_3$) transition; and noticeably, no obvious signals were observed between B1s → π* ($BN_2O$) and B1s → π* ($BO_3$) transition peaks, suggesting that there are negligible conjugated and bridged B-O-B chains formed in the boron oxynitride. This is in accordance with the theoretical predictions. Furthermore, O K-edge XANES reveals the transitions originated from O1s → π* ($OHB_2$) and π* ($OB_3$), which are located at 528.9 and 533.8 eV, respectively; these are very different with the O K-edge structures of a $B_2O_3$ compound[30]. The recorded B1s peak (Fig. S5) can be fitted with two modes located at 190.8 eV and 191.8 eV. The former peak derives from the main $BN_3$ component[31], whereas the latter is caused by the presence of an oxygen-substituted $BN_2O$ structure, which possesses peaks ~1-2 eV lower than those peculiar to $B_2O_3$ or boric acid[32].

**Magnetic properties of boron oxynitride**

Unpaired electrons and corresponding paramagnetism are expected along with the substitution of N with O atoms in a *h*-BN lattice. Strong EPR resonance signal was indeed detected at a

magnetic field of ~320 mT with the calculated g-value of 2.0034. This demonstrates the existence of free electrons in the synthesized BNO material (Fig. 3). As a comparison, no such resonance peak was found for a standard *h*-BN compound. Only isolated conjugated $B_3O$ structures can induce paramagnetic signatures of the material. Other structures, such as O-B-O chains and the –OH groups bonded at the BN monolayer edges, are not able to generate the unpaired electrons and, thus, paramagnetic properties. Substituted O-atom has one extra electron in comparison with N-atom, which results in the presence of unpaired electron after the in-plane bonding with B-atoms in a BNO nanosheet. To confirm such point, we calculated deformation charge density, *i.e.* difference between the valence charge density and the sum of atomic valence charge densities, for a BNO nanoflake with 25 at.% oxygen. In Fig. 3b, the mapped plane profile of the deformation charge density shows localized negative charges around the O dopants of the BNO nanosheet, which are caused by the injection of extra electrons into the conjugated π bonds from the O atoms with respect to the removed N atoms. .Furthermore, simulated electron spin density is mainly presented in the HOMO orbital after introduction of an oxygen atom into the edge –OH terminated BNO nanosheet (Supplementary Fig. S9). Thus, the formation of B-O conjugated structures through the replacement of N atoms is evident. And they result in paramagnetic properties of the synthesized boron oxynitride material.

**Optical band gaps of boron oxynitride**

The BNO optical absorptions change remarkably as compared with the standard *h*-BN; the latter has optical absorptions only at the very deep UV range (⩽230 nm) in accord with the derived band gap value of 5.4 eV. As shown in Fig. 4a, the prepared BNO exhibits strong absorptions within the whole UV range (<400 nm), violet and blue light ranges, and shows the absorption onset at ~800 nm. The estimated optical band gap of this yellow BNO compound is 2.1 eV.

Furthermore, photoluminescence (PL) spectroscopy was also employed to understand the optical band gap properties of the regarded BNO material. It is known that highly pure *h*-BN does not exhibit visible photoluminescence owing to its wide band gap. Usually, the reported PL of *h*-BN materials have been associated with the electronic property changes due to defects[33-35]. As shown in Fig 4a, for the present case, there are two main emission bands in their PL spectra under different excitation wavelengths, from 320 to 390 nm: namely at 415 and 440-446 nm, together with a shoulder band located at 505-510 nm. These PL emission peaks correspond to the recombination energies of 3.0, 2.8 and 2.4 eV, proving the corresponding energy gaps between the LUMO and occupied band states (Fig. 4d). Thus, this BNO compound should be a cyan phosphor material (Fig. 4a). The recorded fluorescence decay curve (Supplementary Fig. S13) measured by time-correlated single photon counting (TCSPC) system can be fitted by the multiple exponential functions with 3 lifetimes: $\tau_1$ = 0.3, $\tau_2$ = 1.9, $\tau_3$ = 6.3 ns, indicating the existence of different relaxation processes. In Supplementary Fig S14, a 2D PL spectrum shows that $\lambda_{em}$ at 440-446 nm is almost constant along with changes of $\lambda_{exc}$, indicating the intrinsic energy gap nature of the

present BNO material.

More interestingly, using 450 and 455 nm excitation wavelengths, we observed anti-Stokes shift photoluminescence located at the higher energy ranges of 415, 435 and 440 nm (Fig. 4c). These anti-Stokes emission bands are in accordance with the Stokes characteristic PL peaks and gain up to 0.26 eV additional energy in their emitting lights. Unlike the Stokes photoexcitation process, electrons in the low-energy-level occupied orbitals can absorb phonons to hop into the high-energy-level occupied orbitals before/together with the photoexcitation and to gain the additional energies for light emissions (Fig. 4d). Such anti-Stokes luminescence phenomena have been reported in a few organic heterocyclic molecules but are still largely unknown for BN and other inorganic nanomaterials[36].

## Discussion

As reported before, treating the BN precursors in ammonia at high temperatures, such as 1000 ℃, is efficient to eliminate the carbonaceous components in the final products[37]. When using primary and secondary amines as the N source, many pure BN materials with diverse structures have been synthesized[38,39]. This is because the reaction energy barrier for the -OH groups of boric acid and the protons in amines to form new B-N bonds is not very high owing to the formation and loss of $H_2O$ molecules under high temperatures. On the other hand, formation of B-N bonds between boric acid and tertiary amine requires overcoming higher energy barriers to eliminate the

attached –OH and other organic groups in amine. Thus, as a result, a high portion of B-O bonds in boric acid is sustained in the final product and yields an oxygen-incorporated BN nanosheet structure where oxygen atoms take the interior in-plane and sheet edge positions.

The intrinsic structural stability of a material is also an important factor for the successful applications. Thus herein, cohesive energies of the proposed 2D periodical BNO structures (with 10 and 20 at.% of oxygen) were calculated. The results show that the cohesive energy is 6.59 eV/atom for the 10 at.% O-doped structure. This is comparable with the standard *h*-BN and larger than that for the 20 at.% O-doped structure, as well as for the reported $MoS_2$ nanosheets and silicene, as described in SI in more detail[40]. Meanwhile, the simulated in-plane Young's modulus of the present BNO nanosheet is also close to that of *h*-BN and higher than those of $MoS_2$ and $WS_2$ nanosheets (see Supplementary Information)[41]. To investigate the thermal stability of the obtained BNO, *ab initio* molecular dynamics simulations (MD) were carried out using 2×2×1 supercells. As shown in Fig. 5a, 5b and Supplementary Movie 1, the periodical BNO structure with 10 at.% of oxygen exhibits excellent thermal stabilities at high temperatures, both at 700 K and 1400 K. While for the 20 at.% O-doped structure, the nanosheet starts to dissociate quickly (from 0.7 ps) owing to instability of O-B-O chains restricted in a honeycomb-like lattice (Fig. 5c, 5d and Supplementary Movie 2).

## Conclusions

Our systematic theoretical studies have predicted that the electronic properties of *h*-BN monoatomic sheets are tunable and their band gap can be narrowed to ~1.7 eV through oxygen doping and/or functionalization. Then, a yellow flake-like BNO compound with an optical band gap of 2.1 eV has successfully been synthesized *via* the reactions of boric acid and tertiary amine. Thorough structural characterization has confirmed the presence of oxygen substitutions for nitrogen atoms within the BN in-plane lattices and the $sp^2$ type hydroxylation at the plane edges. And for the first time, the long-sought magnetic property tuning of the *h*-BN layers through oxygen functionalization has been demonstrated in the experiment. These findings pave the new way for *h*-BN nanosheet optical, electronic and magnetic property engineering, and should breed brand-new applications of layered BN materials in optical, electrical, information and energy-related fields.

## Methods

### Theoretical calculations

All calculations of the atomic structure and electronic properties were performed using DFT-PAW formalism[42], as implemented in the Vienna *ab-initio* Simulation Package (VASP)[43,44]. The plane-wave energy cutoff was equal to 450 eV. The active frequencies of IR spectra were calculated using DFPT phonon calculations. Test calculations of IR active frequencies of pure *h*-BN display the values of 796.9 $cm^{-1}$ and 1346.5 $cm^{-1}$ which are in a good agreement with the

earlier experimental results (802.23 $cm^{-1}$ and 1365 $cm^{-1}$)[45]. The atom projections on the band structure were obtained with the aid of the "Pymatgen Python" library for materials analysis[46]. To calculate the equilibrium atomic structures, the Brillouin zone was sampled according to the Monkhorst–Pack scheme[47] with a 6×6×1 *k*-point convergence grid. To avoid the spurious interactions between the neighboring images along the Z direction, the vacuum space between them was set larger than 15 Å. The structural relaxation was performed until the forces acting on each atom became less 0.001 eV/Å. Calculations of charge density were carried out using DFT with the general gradient approximation (DFT-PBE) implemented in the SIESTA package[48]. Elastic moduli and cohesive energy calculations were also carried out (the details are shown in Supplementary Information). *Ab initio* molecular dynamics simulations were additionally performed to study thermal stability of BNO nanosheets. We applied ABMD for BNO nanosheets with 10 and 20 at.% of oxygen, as well as for oxynitride nanoflakes with the same oxygen concentration. For BNO nanosheets a 2×2×1 supercell was used. The molecular dynamics simulations were carried out at a constant temperature using the Nosé–Hoover thermostat[49,50]. Temperatures were set at 700 K and 1400 K. The total time of the simulations was fixed to 5 ps with the time steps equal to 1 fs. Atomic structure was recorded after every 10 ionic steps.

**Synthesis and characterizations of boron oxynitride**

20 mmol $H_3BO_3$ and 40 mmol hexamethylenetetramine (HMTA) were mixed in ~100 mL hot DI water under stirring to form a clear solution. Then, water was evaporated at ~90 ℃ to recover

the solid $H_3BO_3$-HMTA mixture as a precursor for the BNO synthesis. The obtained precursor was loaded in a horizontal quartz tube and heated at 1000 ℃ for 3 h at a heating rate of 10 $^{o}$C min$^{-1}$ in ammonia atmosphere. After the reaction, the furnace was cooled to room temperature naturally. The prepared yellow powders were collected and suspended in ~80 ℃ DI water under stirring overnight to dissolve possible boron oxide byproducts. Finally, the product was collected under membrane filtering and completely dried at 175 ℃ and $10^{-2}$ Pa for further characterizations and property studies.

The morphology of the materials was characterized by a JEOL JSM-6700 SEM and JEOL JEM-3000F TEM. Compositions of the materials were qualitatively analyzed by EDX (JEOL) and EELS (Gatan 766 2D-DigiPEELS) techniques, and quantitatively determined using ICP-OES for B, carbon/sulfur determinator for C, and oxygen/nitrogen determinator for N and O. XRD measurements were carried out on a Rigaku Ultima III diffractometer (Cu Kα). $N_2$ adsorption and desorption isotherms were taken on a Quantachrome Autosorb-iQ system at −196 °C. Further calculations of the material BET specific surface areas (SSAs), pore size distributions and other textural properties were made. FT-IR spectra were collected on a Nicolet 4700 FT-IR spectrophotometer. X-ray Absorption Near Edge Structure (XANES) data was collected on the 4B7B beamline at the Beijing Synchrotron Radiation Facility (BSRF) using total electron yield (TEY) mode. The electron energy was 2.5 GeV and the beam current was 150–250 mA. XPS was measured using a PHI Quantera SXM system. UV/Vis spectra were collected in a JASCO V-570

UV/Vis/NIR spectrophotometer in a diffuse reflection mode, while the photoluminescence spectra were recorded in a Hitachi F-7000 system. The powder samples were pressed on a quartz window to a thickness of ~1 mm for both UV/Vis/NIR and photoluminescence measurements. EPR spectra were recorded at a JEOL JES RE-1X spectrometer (X-band), $Mn^{2+}$/MgO was taken as a standard marker for magnetic field calibration.

## References


1. Novoselov, K. S., Mishchenko, A., Carvalho, A. & Castro Neto, A. H. 2D materials and van der Waals heterostructures. *Science* **353**, aac9439 (2016).
2. Liu, J., Wang, H., & Antonietti, M. Graphitic carbon nitride "reloaded": emerging applications beyond (photo)catalysis. *Chem. Soc. Rev.* **45**, 2308–2326 (2016).
3. Chhowalla, M. *et al.* The chemistry of two-dimensional layered transition metal dichalcogenide nanosheets. *Nat. Chem.* **5**, 263–275 (2013).
4. Schubert, E. F. *Doping in III-V Semiconductors*. (Cambridge University Press, 2005).
5. Ci, L. *et al.* Atomic layers of hybridized boron nitride and graphene domains. *Nat. Mater.* **9**, 430–435 (2010).
6. Levendorf, M. P. *et al.* Graphene and boron nitride lateral heterostructures for atomically thin circuitry. *Nature* **488**, 627–632 (2012).
7. Lu, J. *et al.* Order–disorder transition in a two-dimensional boron–carbon–nitride alloy. *Nat. Commun.* **4**, 2681 (2013).
8. Weng, Q., Wang, X., Wang, X., Bando, Y. & Golberg, D. Functionalized hexagonal boron nitride nanomaterials: emerging properties and applications. *Chem. Soc. Rev.* **45**, 3989–4012 (2016).

9. Silva, L. D. A., Guerini, S. C., Lemos, V. & Filho, J. M. Electronic and structural properties of oxygen-doped BN nanotubes. *IEEE Trans. Nanotechnol.* **5**, 517–522 (2006).

10. Wu, J. & Zhang, W. Tuning the magnetic and transport properties of boron-nitride nanotubes via oxygen-doping. *Solid State Commun.* **149**, 486–490 (2009).

11. Gou, G. Pan, B. & Shi, L. The nature of radiative transitions in O-doped boron nitride nanotubes. *J. Am. Chem. Soc.* **131**, 4839–4845 (2009).

12. Liu, L., Sham, T. K. & Han, W. Investigation on the electronic structure of BN nanosheets synthesized via carbon-substitution reaction: the arrangement of B, N, C and O atoms. *Phys. Chem. Chem. Phys.* **15**, 6929–6934 (2013).

13. Dai, X. J. *et al.* Controlled surface modification of boron nitride nanotubes. *Nanotechnology* **22**, 245301 (2011).

14. Krivanek, O. L. *et al.* Atom-by-atom structural and chemical analysis by annular dark-field electron microscopy. *Nature* **464**, 571–574 (2010).

15. Singh, R. S. *et al.* Band gap effects of hexagonal boron nitride using oxygen plasma. *Appl. Phys. Lett.* **104**, 163101 (2014).

16. Lee, D. *et al.* Scalable exfoliation process for highly soluble boron nitride nanoplatelets by hydroxide-assisted ball milling. *Nano Lett.* **15**, 1238–1244 (2015).

17. Weng, Q. *et al.* Design of BN porous sheets with richly exposed (002) plane edges and their application as $TiO_2$ visible light sensitizer. *Nano Energy* **16**, 19–27 (2015).

18. Tang, C. *et al.* Fluorination and electrical conductivity of BN nanotubes. *J. Am. Chem. Soc.* **127**, 6552–6553 (2005).

19. Li, X. X., Zhao, J. & Yang, J. L. Semihydrogenated BN sheet: a promising visible-light driven photocatalyst for water splitting. *Sci. Rep.* **3**, 1858 (2013).

20. Blase, X., Rubio, A., Louie, S. G. & Cohen, M. L. Quasiparticle band structure of bulk hexagonal boron nitride and related systems. *Phys. Rev. B*: *Condens. Matter Mater. Phys.* **51**, 6868 (1995).

21. Bhattacharya, A., Bhattacharya, S. & Das, G. P. Band gap engineering by functionalization of BN sheet. *Phys. Rev. B: Condens. Matter Mater. Phys.* **85**, 035415 (2012).

22. Hasnip, P. *et al*. Density functional theory in the solid state. *Philos. Trans. A: Math. Phys. Eng. Sci.* **372**, 20130270 (2014).

23. Sota, H. *et al.* Optical and electrical properties of boron nitride oxide films. *Diamond Relat. Mater.* **17**, 826–829 (2008).

24. Han, W. Q. *et al.* Isotope effect on band gap and radiative transitions properties of boron nitride nanotubes. *Nano Lett.* **8**, 491–494 (2008).

25. Weng, Q. *et al*. Highly water-soluble, porous, and biocompatible boron nitrides for anticancer drug delivery. *ACS Nano* **8**, 6123–6130 (2014).

26. Weng, Q., Wang, X., Zhi, C., Bando Y. & Golberg, D. Boron nitride porous microbelts for hydrogen storage. *ACS Nano* **7**, 1558–1565 (2013).

27. Weng, Q., Wang, X., Bando, Y. & Golberg, D. One-step template-free synthesis of highly porous boron nitride microsponges for hydrogen storage. *Adv. Energy Mater.* **4**, 1301525 (2014).

28. Moon, O., Kang, B., Lee, S. & Boo, J. Temperature effect on structural properties of boron oxide thin films deposited by MOCVD method. *Thin Solid Films* **464**, 164–169 (2004).

29. Zhi, C., Hanagata, N., Bando, Y. & Golberg, D. Dispersible shortened boron nitride nanotubes with improved molecule-loading capacity. *Chem. Asian J.* **6**, 2530–2535 (2011).

30. Liu, L., Sham, T., Han, W., Zhi, C. & Bando, Y. X-ray ecited optical luminescence from hexagonal boron nitride nanotubes: electronic structures and the role of oxygen impurities. *ACS Nano* **5**, 631–639 (2011).

31. Gouin X., Grange P., Bois L., L'Haridon P. & Laurent Y. Characterization of the nitridation process of boric acid. *J. Alloys Compd.* **224**, 22–28 (1995).

32. Joyner D.J. & Hercules D.M., Chemical bonding and electronic structure of $B_2O_3$, $H_3BO_3$, and BN: An ESCA, Auger, SIMS, and SXS study. *J. Chem. Phys.* **72**, 1095 (1980).

33. Tran, T. T., Bray, K., Ford, M., Toth, M. & Aharonovich, I. Quantum emission from hexagonal boron nitride monolayers, *Nat. Nanotech.* **11**, 37–41 (2016).
34. Zhang, X. *et al.* Effects of carbon and oxygen impurities on luminescence properties of BCNO phosphor. *J. Am. Ceram. Soc.* **97**, 246–250 (2014).
35. Zhang, X. *et al.* Blue emitting BCNO phosphors with high quantum yields. *J. Mater. Chem. C*, **3**, 3311–3317 (2015).
36. Zhu, X., Su, Q., Feng, W. & Li, F. Anti-Stokes shift luminescent materials for bio-applications , *Chem. Soc. Rev.* DOI: 10.1039/C6CS00415F (2017).
37. Schlienger, S. *et al.* Micro-, mesoporous boron nitride-based materials templated from zeolites. *Chem. Mater.* **24**, 88–96 (2012).
38. Nag, A. *et al.* Graphene analogues of BN: novel synthesis and properties. *ACS Nano* **4**, 1539–1544 (2010).
39. Lei, W., Portehault, D., Liu, D., Qin, S. & Chen, Y. Porous boron nitride nanosheets for effective water cleaning. *Nat. Commun.* **4**, 1777 (2013).
40. Calculated cohesive energy values for boron oxynitride, as well as the comparison with those of other reported 2D materials, are listed in the Supplementary Information.
41. Detailed calculations of Young's modulus for boron oxynitride and other 2D materials are presented and discussed in the Supplementary Information.
42. Blöchl, P. E. Projector augmented-wave method. *Phys. Rev. B: Condens. Matter Mater. Phys.* **50**, 17953–17979 (1994).
43. Kresse, G. & Furthmüller, J. Efficiency of *ab-initio* total energy calculations for metals and semiconductors using a plane-wave basis set. *Comput. Mater. Sci.* **6**, 15–50 (1996).
44. Kresse, G. & Furthmüller, J. Efficient iterative schemes for *ab initio* total-energy calculations using a plane-wave basis set. *Phys. Rev. B: Condens. Matter Mater. Phys.* **54**, 11169–11186 (1996).
45. Hidalgo, A., Makarov, V., Morell, G. & Weiner, B. R. High-yield synthesis of cubic and

hexagonal boron nitride nanoparticles by laser chemical vapor decomposition of borazine. *Dataset Pap. Sci.* **2013**, e281672 (2012).

46. Ong, S. P. *et al.* Python materials genomics (pymatgen): a robust, open-source python library for materials analysis. *Comput. Mater. Sci.* **68**, 314–319 (2013).

47. Monkhorst, H. J. & Pack, J. D. Special points for Brillouin-zone integrations. *Phys. Rev. B: Condens. Matter Mater. Phys.* **13,** 5188–5192 (1976).

48. Soler, J. M.; Artacho, E.; Gale, J. D.; García, A.; Junquera, J.; Ordejón, P.; Sánchez-Portal, D. The Siesta method for ab initio-order-materials simulation. *J. Phys.: Condens. Mat.* **14**, 2745–2779 (2002).

49. Nosé, S. A unified formulation of the constant temperature molecular dynamics methods. *J. Chem. Phys.* **81,** 511–519 (1984).

50. Hoover, W. G. Canonical dynamics: Equilibrium phase-space distributions. *Phys. Rev. A* **31,** 1695–1697 (1985).

## Acknowledgements

This work was supported by the World Premier International Center for Materials Nanoarchitectonics (WPI-MANA) of NIMS, Tsukuba, Japan and JSPS KAKENHI Grant (16K21600). D. G. K. and P. B. S. are gratefully acknowledge the financial support of the Ministry of Education and Science of the Russian Federation in the framework of Increase Competitiveness Program of NUST «MISiS»(№ К2-2015-033).

## Author contributions

Q. H. W. performed boron oxynitride synthesis and characterizations. D. K. performed theoretical simulations. X. W. and Y. Y. collected the XANES data. Q. H. W. and D. K. wrote the manuscript.

O. C., M. Z. C. C. Z. and D.-M. T. participated in the experiments. P. B. S. and D. G. K. were involved in the discussion of the theoretical part. All authors participated in the data analysis and result discussions. D. G. revised the manuscript and supervised the whole project.

## Additional information

The authors declare no competing financial interests. Supplementary information accompanies this paper on www.nature.com/naturecommunications. Reprints and permissions information is available on line at http://npg.nature.com/reprintsandpermissions.

## Figure legends

**Figure 1 | Theoretical simulations of electronic properties for boron oxynitride nanosheets. (a)** Calculated density of states (DOS) of a pure *h*-BN monolayer. **(b)** Dependence of the band gap on the embedded oxygen content (random doping mode) in an infinite *h*-BN monolayer. **(c)** DOS profile of a BNO nanosheet with the edges functionalized with conjugated –OH groups (12.5 at.% oxygen). **(d)** DOS profile of a BNO nanosheet with the edges functionalized with conjugated –OH groups and with interior substituted oxygen atoms. The inset is the structural model having in total 25 at.% O-atoms.

**Figure 2 | Microscopic and spectroscopic characterizations of the synthesized yellow boron oxynitride. (a)** TEM image of the synthesized BNO material. **(b)** High-resolution TEM image. The inset in **b** is the contrast intensity profile from the position marked with a blue dashed line. **(c)**

EDX spectrum of the sample with a quantitative elemental composition data shown in the inset. The elemental compositions are measured by independent methods for B, C and N/O, as described in the experimental section. **(d)** XRD pattern of a BNO sample. **(e)** Comparison of the measured FT-IR spectrum with the DFT-simulated curve. DFT simulation is based on a 2D periodical BNO nanosheet model with 10 at.% of oxygen dopants. **(f)** B and O K-edge X-ray Absorption Near-Edge Structure (XANES) spectra.

**Figure 3 | Magnetic properties of boron oxynitride (BNO). (a)** Comparison of EPR spectra of synthesized BNO material and *h*-BN powders. The asterisks marked in the figure are the $Mn^{2+}$ label signals. **(b)** Deformation charge density distribution in a BNO nanosheet with 25 at.% of oxygen doping and edge functionalization. The unit of charge density is e/Å$^3$; the colours for atomic species are depicted in the insets.

**Figure 4 | Optical absorption, photoluminescence (PL) and anti-Stokes photoluminescence properties. (a)** Kubelka-Munk plots of UV/Vis/NIR spectrum of the synthesized BNO in comparison with standard *h*-BN powders. The measured optical band gaps for BNO and *h*-BN are 2.1 and 5.4 eV, respectively. The inset is a photograph of the synthesized BNO sample. **(b)** PL emission spectra of a BNO sample under different excitation wavelengths. The inset shows cyan luminescent characters “NIMS” written with BNO powders and under UV light irradiations (275

nm< λ <375 nm). **(c)** Anti-stokes photoluminescence spectra of BNO excited at wavelengths of 450 and 455 nm, respectively. There are 10-40 nm blue shifts toward higher energies. **(d)** Schematic illustrations of the observed PL and anti-Stokes PL phenomena for the BNO sample.

**Figure 5 | Thermal stabilities of boron oxynitride. (a)** Simulated structure of a 2D periodical BNO nanosheet with 10 at.% of oxygen atoms after molecular dynamics annealing at 1400 K for 5 ps. **(b)** Fluctuation of potential energy (2×2×1 supercell) during NVT *ab initio* MD simulation at 700 K (blue curve) and 1400 K (red curve), **(c)** Simulated structure of a 2D BNO nanosheet with 20 at.% of oxygen dopants after molecular dynamics annealing at 700 K for 1.2 ps. **(d)** Fluctuation of the potential energy (2×2×1 supercell) during NVT *ab initio* MD simulation at 700 K. The colours for atom species in **(a)** and **(c)** are red for B, green for N, and blue for O.

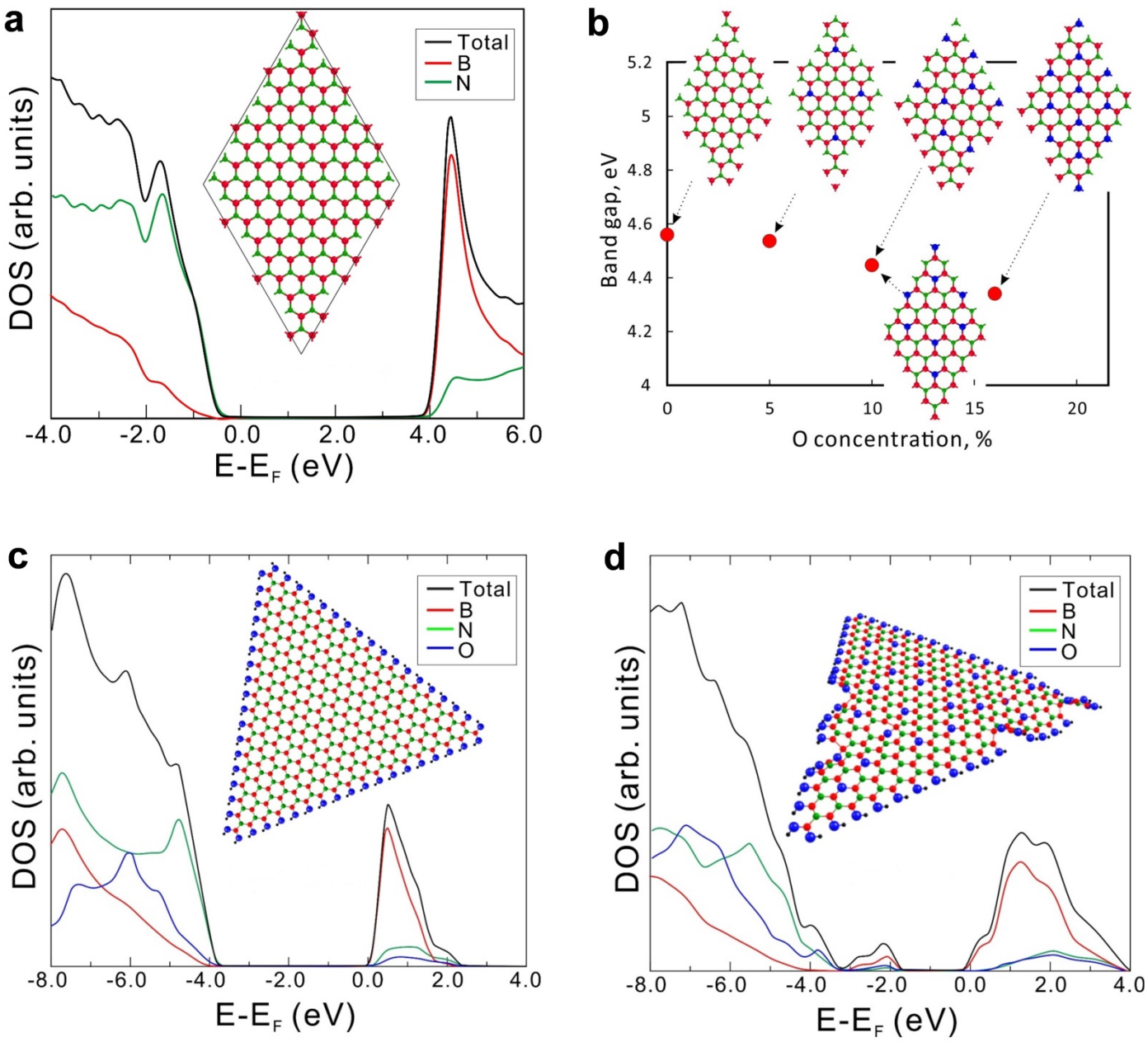
a
Total
B
N
DOS (arb. units)
-4.0
-2.0
0.0
2.0
4.0
6.0
E-E$_F$ (eV)
b
5.2
5
4.8
4.6
4.4
4.2
4
Band gap, eV
0
5
10
15
20
O concentration, %
c
Total
B
N
O
DOS (arb. units)
-8.0
-6.0
-4.0
-2.0
0.0
2.0
4.0
E-E$_F$ (eV)
d
Total
B
N
O
DOS (arb. units)
-8.0
-6.0
-4.0
-2.0
0.0
2.0
4.0
E-E$_F$ (eV)

**Figure 1**

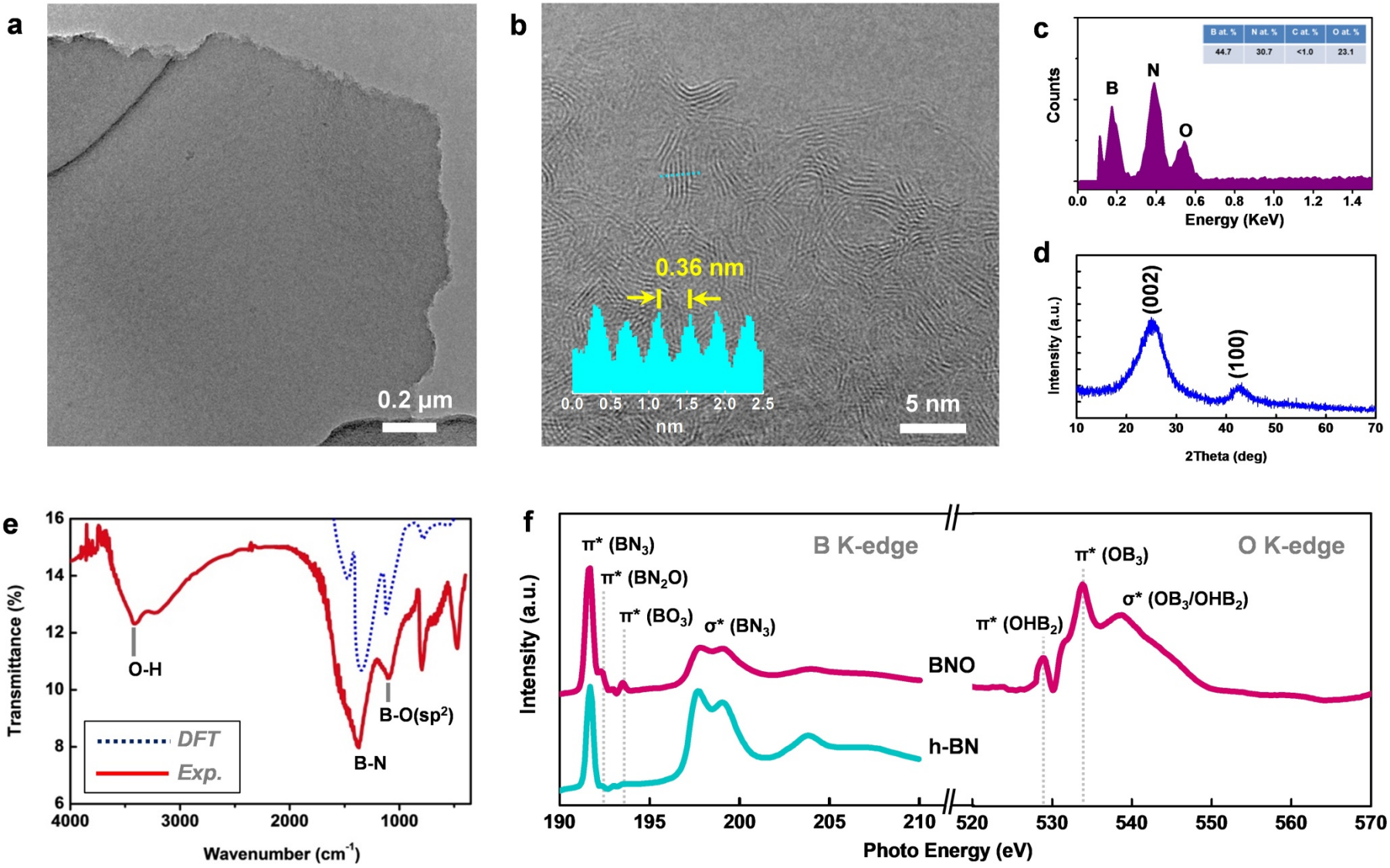
a
0.2 μm
b
0.36 nm
0.0 0.5 1.0 1.5 2.0 2.5
nm
5 nm
c
B at. %
N at. %
C at. %
O at. %
44.7
30.7
<1.0
23.1
B
N
O
Counts
0.0 0.2 0.4 0.6 0.8 1.0 1.2 1.4
Energy (KeV)
d
(002)
(100)
Intensity (a.u.)
10 20 30 40 50 60 70
2Theta (deg)
e
Transmittance (%)
16 14 12 10 8 6
O-H
B-O(sp²)
B-N
DFT
Exp.
4000 3000 2000 1000
Wavenumber (cm⁻¹)
f
π* (BN₃)
π* (BN₂O)
π* (BO₃)
σ* (BN₃)
B K-edge
O K-edge
π* (OB₃)
σ* (OB₃/OHB₂)
π* (OHB₂)
BNO
h-BN
Intensity (a.u.)
190 195 200 205 210 520 530 540 550 560 570
Photo Energy (eV)

**Figure 2**

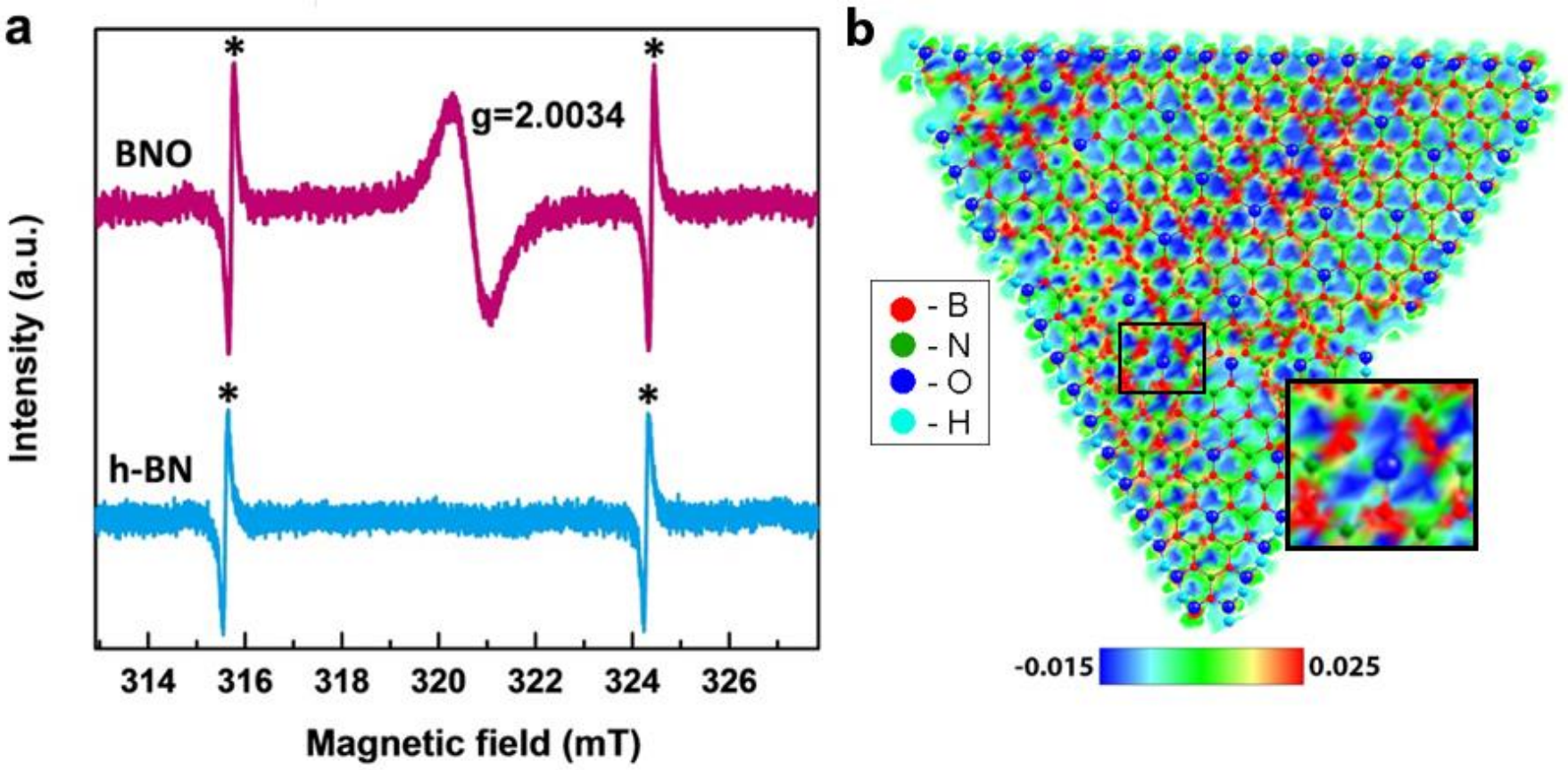
a
b
BNO
h-BN
g=2.0034
*
Intensity (a.u.)
314
316
318
320
322
324
326
Magnetic field (mT)
- B
- N
- O
- H
-0.015
0.025

**Figure 3**

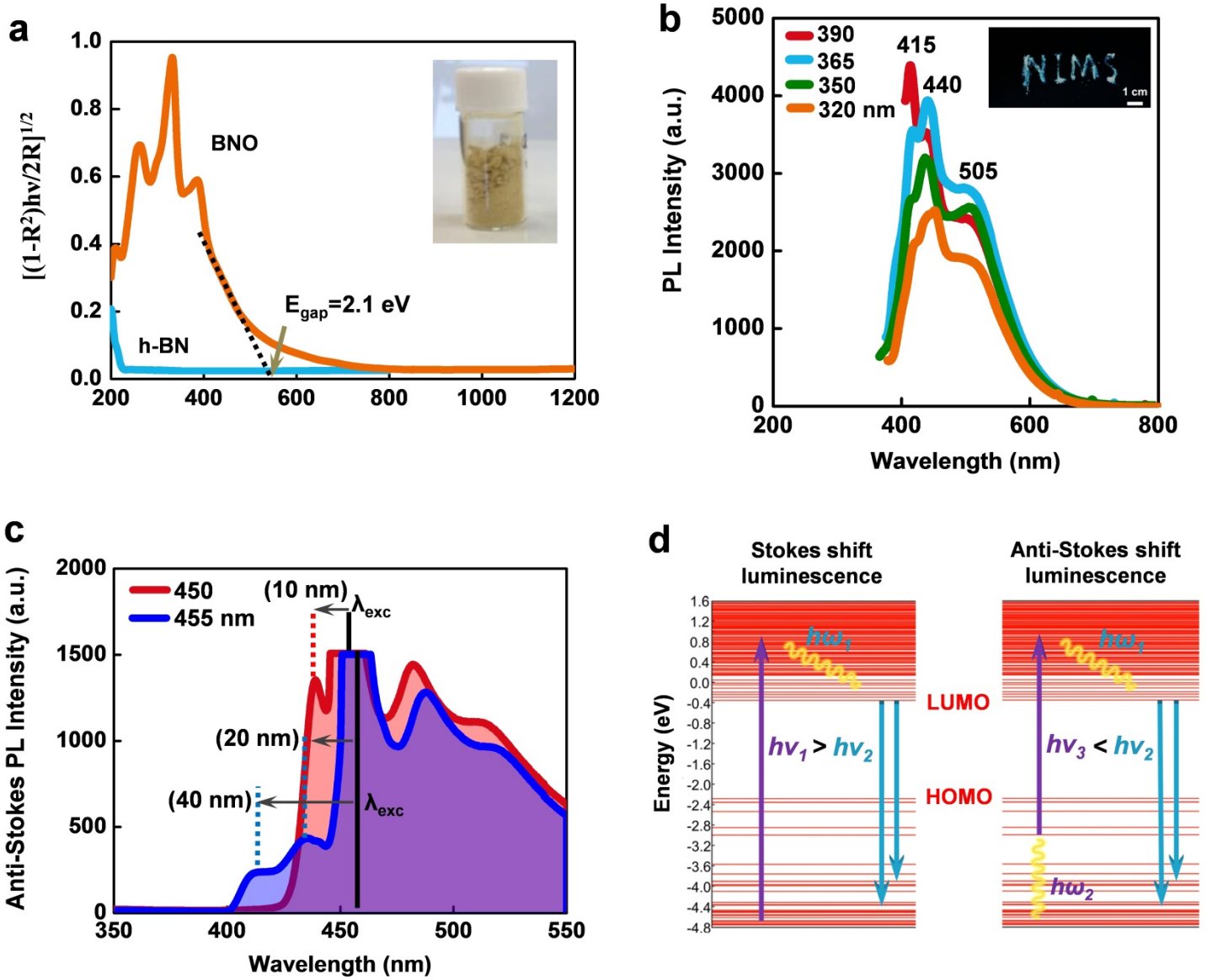
a
[(1-R²)hν/2R]^1/2
BNO
h-BN
E_gap=2.1 eV
b
PL Intensity (a.u.)
Wavelength (nm)
390
365
350
320 nm
415
440
505
NIMS
1 cm
c
Anti-Stokes PL Intensity (a.u.)
Wavelength (nm)
450
455 nm
(10 nm)
(20 nm)
(40 nm)
λexc
d
Stokes shift luminescence
Anti-Stokes shift luminescence
Energy (eV)
LUMO
HOMO
hν1
hν2
hν1 > hν2
hν3 < hν2

Figure 4

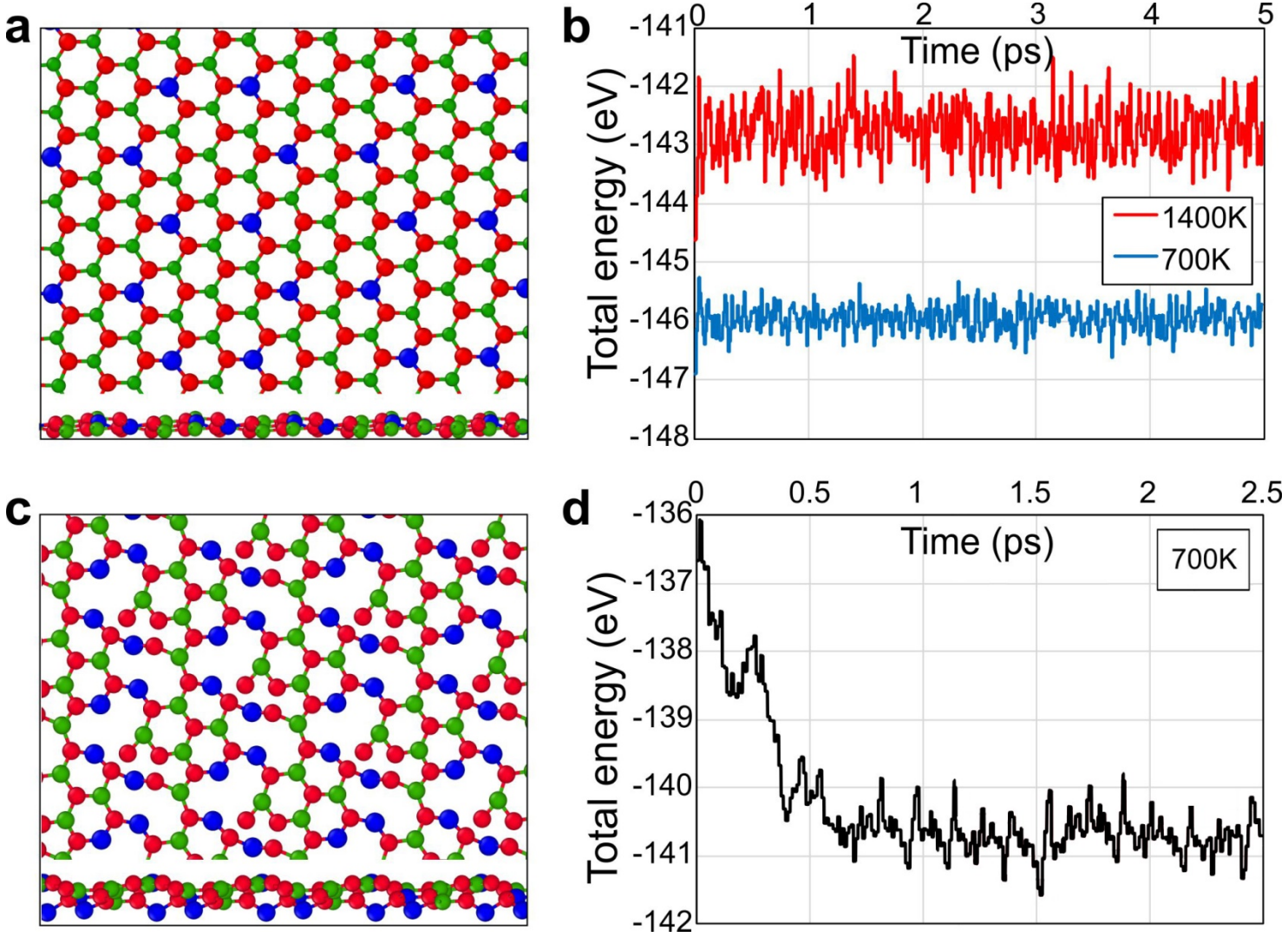
a
b
Time (ps)
Total energy (eV)
1400K
700K
c
d
Time (ps)
Total energy (eV)
700K

**Figure 5**